Advanced Powder Technology 28 (2017) 1008–1017

Contents lists available at ScienceDirect

Advanced Powder Technology

journal homepage: www.elsevier.com/locate/apt

Original Research Paper

MHD heat and mass transfer flow of a nanofluid over an inclined vertical porous plate with radiation and heat generation/absorption

P. Sudarsana Reddy [a], Ali J. Chamkha [b,c,*], Ali Al-Mudhaf [d]

[a] Department of Mathematics, RGM College of Egg. & Tech, Nandyal 518501, AP, India
[b] Mechanical Engineering Department, Prince Mohammad Bin Fahd University, Al-Khobar 31952, Saudi Arabia
[c] Prince Sultan Endowment for Energy and Environment, Prince Mohammad Bin Fahd University, Al-Khobar 31952, Saudi Arabia
[d] Manufacturing Engineering Department, The Public Authority for Applied Education and Training, Shuweikh 70654, Kuwait

ARTICLE INFO

Article history:
Received 31 August 2016
Received in revised form 21 December 2016
Accepted 8 January 2017
Available online 23 January 2017

Keywords:
Nanofluid
Inclined plate
MHD
Radiation
Heat source/sink
Finite element method

ABSTRACT

MHD boundary layer flow, heat and mass transfer analysis of nanofluid over an inclined vertical plate saturated by porous medium with thermal radiation, magnetic field and heat generation/absorption is investigated in the present article. By using similarity variables the governing non-linear partial differential equations are transformed into ordinary differential equations and these equations together with associated boundary conditions are solved numerically by using versatile, extensively validated, variational Finite element method. The sway of key parameters, such as, Magnetic parameter (M), buoyancy ratio parameter (Nr), Radiation parameter (An), Heat source/sink parameter (Q), Brownian motion parameter (Nb), thermophoretic parameter (Nt) and Lewis number (Le) on hydrodynamic, thermal and concentration boundary layers are examined in detail and the results are shown graphically. Furthermore, the impact of these parameters on local skin friction coefficient (C_f), rate of heat transfer (Nu_x) and rate of mass transfer (Sh_x) is also investigated. The results are compared with the works published previously and found to be excellent agreement.

1. Introduction

A nanofluid is a fluid containing small volumetric quantities of nanometer-sized (diameter of about 1–100 nm) particles called nanoparticles. The nanoparticles used in nanofluids are naturally made of metals (Cu, Al), (or) oxides (TiO_2, Al_2O_3, CuO, SiO_2), carbides (SiC), nitrides (SiN, AlN), (or) nonmetals (graphite, carbon nanotubes). The convectional heat transfer fluids like water, oil and ethylene glycol mixture have low heat transfer abilities due to their less thermal conductivity. In general, the thermal conductivity of the metals is three times more than that of general fluids, so it is admissible to mix the two substances to produce a heat transfer medium that behaves like a fluid but has the metal's thermal conductivity. To improve the thermal conductivity of these fluids nano/micro-sized particle materials are suspended in liquids. Several theoretical and experimental investigations have been made to enhance the thermal conductivity of these fluids; Choi [1] was the first among all who introduced a new type of fluid called nanofluid while doing research on new coolants and cooling technologies. Eastman et al. [2] have noticed in an experiment that the thermal conductivity of the base fluid (water) has increased up to 60% when CuO nanoparticles are added to the base fluid with volume fraction 5%. This enhancement is because of increasing surface area of the base fluid due to the suspension of nanoparticles. Eastman et al. [3] have revealed that the thermal conductivity has increased 40% when copper nanoparticles with the volume fraction less than 1% are added to the ethylene glycol or oil. Choi et al. [4] have reported that there is 150% enhancement in the thermal conductivity when carbon nanotubes are added to the ethylene glycol or oil. In addition, Xie et al. [5] have observed that Al_2O_3- ethylene glycol based nanofluid thermal conductivity is increased in the range 25–30% when Alumina nanoparticles are added. Buongiorno [6] has reported in his bench mark study using scale analysis that, there are seven possible mechanisms which increases the thermal conductivity of the nanofluid, such as, nanoparticle size, inertia, particle agglomeration, Magnus effect, volume fraction of the nanoparticle, Brownian motion and thermophoresis. Among all these they found that Brownian motion and thermophoresis are significant slip mechanisms in nanofluids.

* Corresponding author at: Mechanical Engineering Department, Prince Mohammad Bin Fahd University, Al-Khobar 31952, Saudi Arabia.
E-mail addresses: sudarsanareddy@rgmcet.edu.in (P. Sudarsana Reddy), achamkha@pmu.edu.sa (A.J. Chamkha), a_fahad@yahoo.com (A. Al-Mudhaf).

http://dx.doi.org/10.1016/j.apt.2017.01.005
0921-8831/

Nomenclature

Sh_x	Sherwood number
K_m	thermal conductivity
C	nanoparticle volume fraction
C_∞	ambient nanoparticle volume fraction
T_w	temperature at the plate
T	temperature on the plate
q_w	wall heat flux
D_B	Brownian diffusion
$f(\eta)$	dimensionless velocity
Nt	thermophoresis parameter
p	pressure
w	Darcy velocity (u, v)
M	magnetic parameter
Ra_x	Darcy-Rayleigh number
Nr	Buoyancy parameter

Greek symbols

μ	viscosity
κ	permeability of porous medium
ρ_f	fluid density
Ψ	stream function
τ	parameter defined by $\varepsilon \frac{(\rho c)_p}{(\rho c)_f}$
$\phi(\eta)$	dimensionless nanoparticle volume fraction
$\theta(\eta)$	dimensionless temperature
α	acute angle of the plate to the vertical
σ^*	Stephan-Boltzmann constant

Subscripts

w	condition on the plate
η	similarity variable

Ra	mixed convention parameter
Nu_x	Nusselt number
C_w	nanoparticle volume fraction on the plate
(x, y)	cartesian coordinates
T_∞	ambient temperature attained
An	radiation parameter
q_m	wall mass flux
D_T	thermophoretic diffusion coefficient
g	gravitational acceleration
Le	Lewis number
Nb	Brownian motion parameter
q_r	thermal radiation
Q	heat source parameter
Pe_x	Peclet number
K^*	mean absorption coefficient
ε	porosity
α_m	parameter defined by $\frac{k_m}{(\rho c)_f}$
ρ_p	nanoparticle mass density
V	kinematic viscosity of the fluid
$(\rho c)_f$	heat capacity of the fluid
β_0	magnetic field strength
$(\rho c)_p$	heat capacity of the nanoparticle
β	volumetric expansion coefficient
σ	electrical conductivity
∞	condition far away from the plate
f	base fluid

We can see many research papers in literature which deals the heat and mass transfer characteristics of nanofluids by considering Brownian motion and thermophoresis effects into the account. Nield and Kuznetsov [7] have discussed the Cheng-Mincowycz problem for natural convection boundary-layer flow in a porous medium saturated nanofluid. Kuznetsov and Nield [8] deliberated the impact of Brownian motion and thermophoresis on natural convection boundary layer flow, heat and mass transfer of a nanofluid past a vertical plate. Khan and pop [9] have discussed boundary layer flow of a nanofluid over a stretching sheet. Chamkha et al. [10] have discussed the impact of heat generation/absorption on mixed convection flow of a nanofluid past a stretching sheet by taking magnetic field, Brownian motion and thermophoresis into the account.

Magneto nanofluids have specific applications in biomedicine, optical modulators, magnetic cell separation, magneto-optical wavelength filters, silk float separation, nonlinear optical materials, hyperthermia, optical switches, drug delivery, optical gratings etc. A magnetic nanofluid has both the liquid and magnetic properties. The used magnetic field influences the suspended particles and reorganizes their concentration in the fluid regime which powerfully influences the heat transfer analysis of the flow. Magneto nanofluids are useful to guide the particles up the blood stream to a tumor with magnets. This is due to the fact that the magnetic nanoparticles are regarded more adhesive to tumor cells than non-malignant cells. Such particles absorb more power than microparticles in alternating current magnetic fields tolerable in humans i.e. for cancer therapy. Sudarsana Reddy et al. [11] have analyzed finite element analysis of unsteady MHD heat and mass transfer flow over stretching sheet with Soret and Dufour effects and non-uniform heat generation/absorption. Hamad et al. [12] have discussed magnetic field effect on free convection flow of a nanofluid over a vertical semi-infinite vertical flat plate. Poornima et al. [13] have presented the effect of radiation on free convective boundary layer flow over a stretching sheet filled with nanofluid by taking magnetic field effect into the account.

Thermal radiation plays very significant role in the surface heat transfer when convection heat transfer is very small. It has applications in manufacturing industries, the design of reliable equipment's, nuclear plants, gas turbines, aircraft, missiles, satellites, space vehicles, space technology and procedure relating high temperature. Gireesha et al. [14] have studied the impact of radiation and heat source/sink on mixed convective Dusty fluid over a stretching sheet. Rashad et al. [15] have reported natural convection boundary layer analysis of micropolar fluid through porous medium with radiation and chemical reaction. Rashidi et al. [16] have presented the effect of thermal radiation on mixed convective flow and heat transfer of Visco-Elastic fluid over porous wedge. Aly [17] has analyzed thermal radiation and magnetic field effect on boundary layer flow of nanofluid over a stretching sheet through porous medium with suction/injection and heat source/sink. Chamkha et al. [18] have deliberated mixed convection flow over a permeable surface embedded in a porous medium with thermal radiation. Chamkha et al. [19] has studied radiation effect on mixed convective flow through porous medium over a wedge filled with nanofluid. Noghrehabadi et al. [20] have presented natural convection flow, heat and mass transfer of nanofluid over a vertical plate. Haile et al. [21] have discussed the heat and mass transfer characteristics of MHD viscous nanofluid past a stretching sheet by considering thermal radiation. Ghalambaz et al. [22] have analyzed natural convection of nanofluid over a continuously heated vertical plate embedded in porous medium. Chamkha et al. [23] have analyzed natural convection Non-Darcy flow of a Non-Newtonian fluid over a cone under the influence of heat and volume fluxes.

Sudarsana Reddy et al. [24,25] have presented MHD natural convection boundary layer flow, heat and mass transfer characteristics of two different nanofluids over a rotating disk, vertical cone, respectively, with chemical reaction.

The problem of boundary layer, heat and mass transfer flows through porous medium over an inclined plate has received much interest in recent years because of its engineering and industrial applications. Chamkha et al. [26] have reported the natural convection from an inclined plate through a variable porosity porous medium with magnetic field and solar radiation. They suggested that increasing the plate inclination angle resist the motion of the fluid which causes an enhancement in the temperature of the fluid. Alam et al. [27] has deliberated the flow, heat and mass transfer analysis over an inclined plate by taking heat generation and thermophoresis. Very recently, Puneet Rana et al. [28] have presented finite element and finite difference numerical solution for mixed convection flow of a nanofluid along a semi-infinite inclined flat plate through porous medium in the presence of Brownian motion and thermophoresis. They reported that temperature and concentration profiles are remarkably influenced with plate inclination parameter. The different aspects and applications of nanofluid flow over various geometries have been investigated by several authors [29–36].

To the ability of authors' knowledge, no studies have been presented in the literature to discuss MHD mixed convection heat and mass transfer characteristics of nanofluid over an inclined vertical flat plate by taking thermal radiation and heat generation/absorption into the account. Hence, we made an attempt to discuss the problem here. The transformed conservation equations with the corresponding boundary conditions are solved numerically by using versatile, extensively validated, variational finite element method.

2. Mathematical analysis

We consider steady, laminar, two dimensional, incompressible, mixed convention flow, heat and mass transfer of a nanofluid over an inclined plate embedded through porous medium, with an acute angle α to the vertical, illustrated in Fig. 1. The two slip effects of Brownian motion and thermophoresis are considered in this problem. The coordinate system is such that x-axis is along the plate in the direction of the motion and y-axis is perpendicular to it. The plate is maintained at constant temperature T_w and concentration C_w. The temperature and concentration of the ambient fluid are assumed to be T_∞ andC_∞, respectively. A constant magnetic field of intensity β_0 is applied in the y-axis direction.

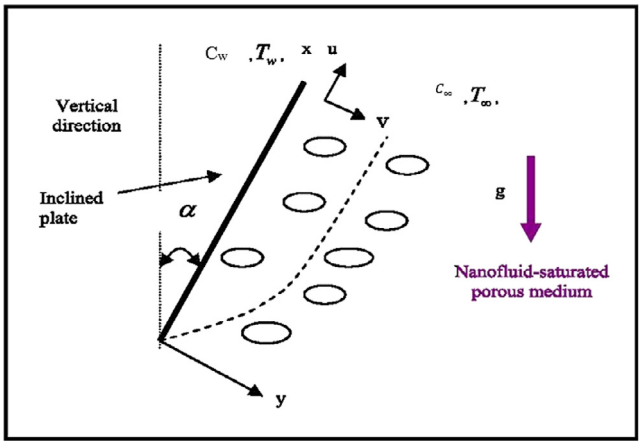

Fig. 1. Physical model and coordinate system.

Imposing magnetic field into the electrically conducting fluid creates a resistive force in the negative x-direction and is called Lorentz force. Based on the reference works of [8,28], by using the Oberbeck-Boussinesq approximation, the governing equations describing the steady-state conservation of mass, momentum, energy as well as conservation of nanoparticles for nanofluids in the presence of thermal radiation and other important parameters take the following form:

$$\frac{\partial u}{\partial x}+\frac{\partial v}{\partial y}=0 \tag{1}$$

$$\frac{\partial p}{\partial y}=0 \tag{2}$$

$$\mu_f\frac{1}{\kappa}u=-\frac{\partial p}{\partial x}+g\left[(1-C_\infty)\rho_{f\infty}\beta(T-T_\infty)-(\rho_p-\rho_{f\infty})(C-C_\infty)\right]\times\cos\alpha-\frac{\sigma\beta_o^2}{\rho_f}u \tag{3}$$

$$\left(u\frac{\partial T}{\partial x}+v\frac{\partial T}{\partial y}\right)=\frac{k_m}{(\rho c_p)_{nf}}\frac{\partial^2 T}{\partial y^2}+\frac{(\rho c)_p}{(\rho c_p)_{nf}}\left[D_B\frac{\partial C}{\partial y}\cdot\frac{\partial T}{\partial y}+\left(\frac{D_T}{T_\infty}\right)\left(\frac{\partial T}{\partial y}\right)^2\right]-Q(T-T_\infty)-\frac{1}{(\rho c_p)_{nf}}\frac{\partial}{\partial y}(q_r) \tag{4}$$

$$\frac{1}{\varepsilon}\left(u\frac{\partial C}{\partial x}+v\frac{\partial C}{\partial y}\right)=D_B\frac{\partial^2 C}{\partial y^2}+\left(\frac{D_T}{T_\infty}\right)\frac{\partial^2 T}{\partial y^2} \tag{5}$$

The boundary conditions based on the problem description are as follows:

$$v=0,\quad T=T_w,\quad C=C_w\quad at\quad y=0 \tag{6}$$

$$u,v\to 0,\quad T\to T_\infty,\quad C\to C_\infty\quad at\quad y\to\infty \tag{7}$$

p may be eliminated from Eqs. (2) and (3) by cross-differentiation and the continuity Eq. (1) will be satisfied introducing a stream function (ψ) defined by the Cauchy-Riemann equations:

$$u=\frac{\partial\psi}{\partial y},\quad v=-\frac{\partial\psi}{\partial x} \tag{8}$$

By substituting, Eq. (8) in Eqs. (3)–(5), we get

$$\frac{\partial^2\psi}{\partial y^2}=\left[\frac{(1-C_\infty)\rho_{f\infty}\beta gk}{\mu}\frac{\partial T}{\partial y}-\frac{(\rho_p-\rho_{f\infty})gk}{\mu}\frac{\partial C}{\partial y}\right]\cos(\alpha)-\frac{\sigma\beta_o^2}{\rho}\frac{\partial\psi}{\partial y} \tag{9}$$

$$\frac{\partial\psi}{\partial y}\frac{\partial T}{\partial x}-\frac{\partial\psi}{\partial x}\frac{\partial T}{\partial y}=\frac{k_m}{(\rho c_p)_{nf}}\frac{\partial^2 T}{\partial y^2}+\frac{\varepsilon(\rho c)_p}{(\rho c_p)_{nf}}\left[D_B\frac{\partial C}{\partial y}\frac{\partial T}{\partial y}+\left(\frac{D_T}{T_\infty}\right)\left(\frac{\partial T}{\partial y}\right)^2\right]-Q(T-T_\infty)-\frac{1}{(\rho c_p)_{nf}}\frac{\partial}{\partial y}(q_r) \tag{10}$$

$$\frac{1}{\varepsilon}\left(\frac{\partial\psi}{\partial y}\frac{\partial C}{\partial x}-\frac{\partial\psi}{\partial x}\cdot\frac{\partial C}{\partial y}\right)=D_B\frac{\partial^2 C}{\partial y^2}+\left(\frac{D_T}{T_\infty}\right)\frac{\partial^2 T}{\partial y^2} \tag{11}$$

The following similarity transformations are introduced to simplify the mathematical analysis of the problem

$$\eta=\frac{y}{x}Pe_x^{1/2},\quad f(\eta)=\frac{\psi}{\alpha_m Pe_x^{1/2}},\quad \theta(\eta)=\frac{T-T_\infty}{T_w-T_\infty},\quad \phi(\eta)=\frac{C-C_\infty}{C_w-C_\infty} \tag{12}$$

where $\alpha_m=\frac{k_m}{(\rho c_p)_{nf}}$.

By using Rosseland approximation for radiation, the radiative heat flux q_r is defined as

$$q_r = -\frac{4\sigma^*}{3K^*}\frac{\partial T^4}{\partial y}, \tag{13}$$

We assume that the temperature differences within the flow are such that the term T^4 may be expressed as a linear function of temperature. This is accomplished by expanding T^4 in a Taylor series about a free stream temperature T_∞ as follows:

$$T^4 = T_\infty^4 + 4T_\infty^3(T - T_\infty) + 6T_\infty^2(T - T_\infty)^2 + \cdots \tag{14}$$

Neglecting higher-order terms in the above Eq. (14) beyond the first degree in $(T - T_\infty)$, we get

$$T^4 \cong 4T_\infty^3 T - 3T_\infty^4. \tag{15}$$

Thus substituting Eq. (15) in Eq. (13), we get

$$q_r = -\frac{16T_\infty^3\sigma^*}{3K^*}\frac{\partial T}{\partial y}. \tag{16}$$

Using the similarity variables (12), Eqs. (9) to (11) together with boundary conditions (6) and (7) reduce to

$$f'' = \frac{Ra_x}{Pe_x}(\theta' - Nr\phi')\cos(\alpha) + Mf' \tag{17}$$

$$\left(1 + \frac{4}{3}An\right)\theta'' + \frac{1}{2}f\theta' + Nb\theta'\phi' + Nt(\theta')^2 - Q\theta = 0 \tag{18}$$

$$\phi'' + \frac{1}{2}Le\, f\, \phi' + \frac{Nt}{Nb}\theta'' = 0 \tag{19}$$

The transformed boundary conditions are

$$\begin{aligned} &\eta = 0, \quad f = 0, \quad \theta = 1, \quad \phi = 1. \\ &\eta = \infty, \quad f' = 1, \quad \theta = 0, \quad \phi = 0. \end{aligned} \tag{20}$$

where prime denotes differentiation with respect to η, and the key thermophysical parameters dictating the flow dynamics are defined by

$$Nr = \frac{(\rho_p - \rho_{f\infty})(C_w - C_\infty)}{\rho_{f\infty}\beta(T_w - T_\infty)(1 - C_\infty)}, \quad Nb = \frac{\varepsilon(\rho c)_p D_B(C_w - C_\infty)}{(\rho c)_f \alpha_m},$$
$$Nt = \frac{\varepsilon(\rho c)_p D_T(T_w - T_\infty)}{(\rho c)_f \alpha_m T_\infty}, \quad Le = \frac{\alpha_m}{\varepsilon D_B},$$
$$Ra_x = \frac{(1 - C_\infty)kg\beta\rho_{f\infty}(T_w - T_\infty)x}{\mu\alpha_m}, \quad Pe_x = \frac{U_\infty x}{\alpha_m}, \quad Ra = \frac{Ra_x}{Pe_x},$$
$$Q = \frac{x^2}{Pe_x\alpha_m}, \quad An = \frac{4T_\infty^3\sigma^*}{K^*\alpha_m}, \quad M = \frac{\sigma\beta_o^2 x}{\rho Pe_x^{1/2}}.$$

Quantities of practical interest in this problem are local Nusselt number (Nu_x), local Sherwood number (Sh_x) are defined as

$$Nu_x = \frac{xq_w}{k(T_w - T_\infty)} \quad Sh_x = \frac{xq_m}{D_B(C_w - C_\infty)} \tag{21}$$

By using the above equations we get the following reduced Nusselt number (Nu_r) and reduced Sherwood number (Sh_r) and are modeled as

$$(Pe_x)^{-1/2}Nu_x = -\theta'(0), \quad (Pe_x)^{-1/2} \quad Sh_x = -\phi\prime(0), \tag{22}$$

Eqs. (17)–(19) are extremely non-linear, so finite-element method [37–40] has been implemented to solve these non-linear equations. The very important aspect in this numerical procedure is to select an approximate finite value of η_∞. So, in order to estimate the relevant value of η_∞, the solution process has been started with an initial value of $\eta_\infty = 4$, and then Eqs. (17)–(19) are solved together with boundary conditions (20). We have updated the value of η_∞ and the solution process is continued until the results are not affected with further values of η_∞ The choice of $\eta_{max} = 8$ *and* $\eta_{max} = 5$ for temperature and concentration have confirmed that all the numerical solutions approach to the asymptotic values at the free stream conditions.

3. Numerical method of solution

3.1. The finite-element method

The finite-element method (FEM) is such a dominant method for solving ordinary differential equations and partial differential equations. The basic idea of this method is dividing the whole domain into smaller elements of finite dimensions called finite elements. This method is such a good numerical method in modern engineering analysis. The steps involved in this method are described below.

(i) Finite-element discretization

In the finite element discretization the entire interval is divided into a finite number of subintervals and this subinterval is called an element. The set of all these elements is called the finite-element mesh.

(ii) Generation of the element equations
   a. Variational formulation of the mathematical model over the typical element (an element from the mesh) is performed.
   b. We assume an approximate solution of the above variational problem, and with the help of this solution we can generate element equations.
   c. Using interpolating polynomials the stiffness matrix is constructed.

(iii) Assembly of element equations

All the algebraic equations are assembled with the help of inter element continuity conditions. This result a large number of algebraic equations called global finite-element model and it represents the whole domain.

(iv) Imposition of boundary conditions

The boundary conditions which represent the flow model are imposed on the assembled equations.

(v) Solution of assembled equations

By using any one of the numerical technique we can solve all the assembled equations.

3.2. Variational formulation

The variational form related with Eqs. (17)–(19) over a typical linear element (η_e, η_{e+1}) is given by

$$\int_{\eta_e}^{\eta_{e+1}} w_1(f'' - Ra(\theta' + Nr\phi')\cos(\alpha) - Mf')d\eta = 0 \tag{23}$$

$$\int_{\eta_e}^{\eta_{e+1}} w_2\left(\left(1 + \frac{4}{3}An\right)\theta'' + \frac{1}{2}f\theta' + Nb\theta'\phi' + Nt(\theta')^2 - Q\theta\right)d\eta = 0 \tag{24}$$

$$\int_{\eta_e}^{\eta_{e+1}} w_3\left(\phi'' + \frac{1}{2}Lef\phi' + \frac{Nt}{Nb}\theta''\right)d\eta = 0 \tag{25}$$

where w_1, w_2, and w_3 are weighted functions and may be regarded as the variations in f, θ, and ϕ, respectively.

3.3. Finite- element formulation

The finite-element form may be attained from above equations by replacing finite-element approximations of the form

$$f=\sum_{j=0}^{3}f_j\psi_j,\quad \theta=\sum_{j=0}^{3}\theta_j\psi_j,\quad \phi=\sum_{j=0}^{3}\phi_j\psi_j \qquad (26)$$

with $w_1=w_2=w_3=\psi_i,\quad (i=1,2,3).$

where Ψ_i are the shape functions for a typical element (η_e,η_{e+1}) and are defined as

$$\psi_1^e=\frac{(\eta_{e+1}+\eta_e-2\eta)(\eta_{e+1}-\eta)}{(\eta_{e+1}-\eta)^2},\quad \psi_2^e=\frac{4(\eta-\eta_e)(\eta_{e+1}-\eta)}{(\eta_{e+1}-\eta)^2},$$
$$\psi_3^e=\frac{(\eta_{e+1}+\eta_e-2\eta)(\eta-\eta_e)}{(\eta_{e+1}-\eta)^2},\quad \eta_e\leqslant\eta\leqslant\eta_{e+1}. \qquad (27)$$

The finite element model of the equations thus formed is given by

$$\begin{bmatrix}[K^{11}] & [K^{12}] & [K^{13}]\\ [K^{21}] & [K^{22}] & [K^{23}]\\ [K^{31}] & [K^{32}] & [K^{33}]\end{bmatrix}\begin{bmatrix}f\\ \theta\\ \phi\end{bmatrix}=\begin{bmatrix}\{r^1\}\\ \{r^2\}\\ \{r^3\}\end{bmatrix}$$

where $[K^{mn}]$ and $[r^m]$ $(m,\ n=1,\ 2,\ 3)$ are defined as

$$K_{ij}^{11}=-\int_{\eta_e}^{\eta_{e+1}}\frac{\partial\psi_i}{\partial\eta}\frac{\partial\psi_j}{\partial\eta}d\eta+M\int_{\eta_e}^{\eta_{e+1}}\psi_i\psi_j d\eta,$$
$$K_{ij}^{12}=-Ra\int_{\eta_e}^{\eta_{e+1}}\psi_i\frac{\partial\psi_j}{\partial\eta}d\eta,$$
$$K_{ij}^{13}=Ra*Nr\int_{\eta_e}^{\eta_{e+1}}\psi_i\frac{\partial\psi_j}{\partial\eta}d\eta.$$
$$K_{ij}^{21}=\frac{1}{2}\int_{\eta_e}^{\eta_{e+1}}\psi_i\bar{\theta}\psi_j d\eta,$$
$$K_{ij}^{22}=\int_{\eta_e}^{\eta_{e+1}}\frac{\partial\psi_i}{\partial\eta}\frac{\partial\psi_j}{\partial\eta}d\eta+Nt\int_{\eta_e}^{\eta_{e+1}}\psi_i\bar{\theta}\frac{\partial\psi_j}{\partial\eta}d\eta+Q\int_{\eta_e}^{\eta_{e+1}}\psi_i\psi_j d\eta$$
$$K_{ij}^{23}=Nb\int_{\eta_e}^{\eta_{e+1}}\psi_i\bar{\theta}\frac{\partial\psi_j}{\partial\eta}d\eta,\quad K_{ij}^{31}=\frac{1}{2}LeNb\int_{\eta_e}^{\eta_{e+1}}\psi_i\bar{\phi}\psi_j d\eta$$
$$K_{ij}^{32}=-Nt\int_{\eta_e}^{\eta_{e+1}}\frac{\partial\psi_i}{\partial\eta}\frac{\partial\psi_j}{\partial\eta}d\eta,\quad K_{ij}^{33}=Nb\int_{\eta_e}^{\eta_{e+1}}\frac{\partial\psi_i}{\partial\eta}\frac{\partial\psi_j}{\partial\eta}d\eta.$$
$$r_i^2=0,\quad r_i^2=-\left(\psi_i\frac{d\psi_i}{d\eta}\right)_{\eta_e}^{\eta_{e+1}},\quad r_i^3=-\left(\psi_i\frac{d\theta}{d\eta}+\frac{d\varphi}{d\eta}\right)_{\eta_e}^{\eta_{e+1}}.$$
$$\text{where, }\bar{f}=\sum_{j=0}^{2}f_i\frac{\partial\psi_i}{\partial\eta}\quad \bar{\theta}=\sum_{j=0}^{2}\theta_i\frac{\partial\psi_i}{\partial\eta},\quad \bar{\varphi}=\sum_{j=0}^{2}\varphi_i\frac{\partial\psi_i}{\partial\eta}.$$

After assembly of element equations, we get the system of strongly non-linear equations and are solved using a robust iterative scheme. The system is linearized by incorporating the functions $\bar{f}$, $\bar{\theta}$ and $\bar{\phi}$, which are assumed to be known. After imposing the boundary conditions, we get the less number of non-linear equations and are solved using Gauss elimination method. The computer program of the algorithm was executed in MATHEMATICA 10.0 running on a PC. To investigate the sensitivity of the solutions to mesh density, we have performed the grid invariance test (Cu – water nanofluid) for temperature and concentration distributions and are shown in Table 1. It is observed from this table that in the same domain the accuracy is not affected, even the number of elements increased, by decreasing the size of the elements.

4. Results and discussion

Comprehensive numerical computations were directed for different values of the key parameters that describe the flow characteristics, and the results are showed graphically and in tabular form. Selected graphical profiles are presented in Figs. 2–18. The results are compared for Nusselt number $(-\theta'(0))$ and Sherwood number $(-\phi'(0))$ with several values of (Le), (Nt) and (Nb) with the works reported by Puneet Rana et al. [28] and are presented in Table 2. Thus, it is seen from Table 1 that the numerical results are in close agreement with those published previously.

The influence of magnetic field parameter (M) on thermal and solutal boundary layers is depicted in Figs. 2 and 3. It is noticed from these figures that the thermal boundary layer thickness as well as the solutal boundary layer thickness enhances with enhance in the values of (M). This is because of the fact that, the presence of magnetic field in an electrically conducting fluid produces a force called Lorentz force, this force acts against the flow direction causes the depreciation in velocity profiles, and at the same time, to overcome the drag force imposed by the Lorentzian retardation the fluid has to perform extra work; this supplementary work can be converted into thermal energy which increases the temperature of the fluid (Fig. 2) and also increases the concentration profiles (Fig. 3).

Figs. 4 and 5 depict the effect of mixed convection parameter Ra $(\frac{Ra_x}{Pe_x})$ on temperature and concentration distributions. It is analyzed that both temperature and concentration profiles decelerates with the increasing values of mixed convection parameter (Ra). This is because of the fact that buoyancy ratio parameter (Nr) influence is less in the boundary layer regime than the mixed convection parameter, so that, there is retardation in the thickness of thermal and solutal boundary layers. Furthermore, the temperature and concentration profiles increase when $Ra=0$ (forced convection) because of no buoyancy forces, and both profiles retards with the increasing values of Ra.

Figs. 6 and 7 illustrate the effect of buoyancy ratio parameter (Nr) on temperature and concentration distributions. The temperature profiles of the fluid increases with the increasing values of buoyancy ratio parameter (Nr). This is from the reality that higher the values buoyancy ratio parameter enhances the fluids temperature, so that thermal boundary layer thickness is increased (Fig. 6). The concentration profiles also enhances throughout the fluid region for different values of the buoyancy ratio parameter (Nr). This is because of the fact that solutal boundary layer thickness elevates with increasing values of (Nr) (Fig. 7).

The variation in temperature and concentration profiles for different values of plate inclination angle (α) is depicted in Figs. 8 and 9. It is noticed from Fig. 8 that, an increase in the plate inclination angle (α) resist the motion of the fluid which causes an enhancement in the temperature of the fluid (Fig. 8). It is also observed that the concentration distributions are increased with increase in the values of (α) (Fig. 9). This elevation in temperature and concentration profiles is because of the reduction in buoyancy ratio term $g[\beta(T-T_\infty)-\beta(C-C_\infty)]\cos(\alpha)$ in the momentum equation with increasing values of α. It is also noticed that the maximum buoyancy force occur for $\alpha=0$ (vertical plate) and there is no buoyancy term when $\alpha=\pi/2$ (horizontal plate). From these two figures we conclude that both thermal boundary layer and solutal boundary layers elevates with the plate inclination angle α.

Temperature and concentration distributions for different values of heat source/sink parameter (Q) are illustrated in Figs. 10 and 11. It is observed that temperature in thermal boundary layer increases with the increase in heat generation parameter$(Q>0)$, whereas thermal boundary layer thickness decelerates with the heat absorption parameter $(Q<0)$ as shown in Fig. 10. This is

Table 1
Grid-invariance test for temperature distribution (θ) and concentration distribution (ϕ) with $M = 0.5$, $Ra = 0.5$, $Nr = 0.5$, $Nt = 0.5$, $Nb = 0.5$, $An = 0.5$, $Le = 10.0$, $Q = 1.0$, $\alpha = \frac{\pi}{6}$.

η	θ Step size (h)				ϕ Step size (h)			
	0.04	0.02	0.01	0.0005	0.04	0.02	0.01	0.0005
0.0	1.0000	1.0000	1.0000	1.0000	1.0000	1.0000	1.0000	1.0000
1.0	0.4359	0.3685	0.2897	0.2547	0.3605	0.3287	0.2854	0.2474
2.0	0.1989	0.1427	0.0953	0.0952	0.0641	0.0452	0.0372	0.0318
3.0	0.0803	0.0612	0.0321	0.0320	0.0154	0.0034	0.0012	0.0010
4.0	0.0318	0.0236	0.0056	0.0051	0.0021	0.0012	0.0001	0.0001
5.0	0.0102	0.0026	0.0012	0.0010	0.0000	0.0000	0.0000	0.0000
6.0	0.0000	0.0000	0.0000	0.0000	–	–	–	–

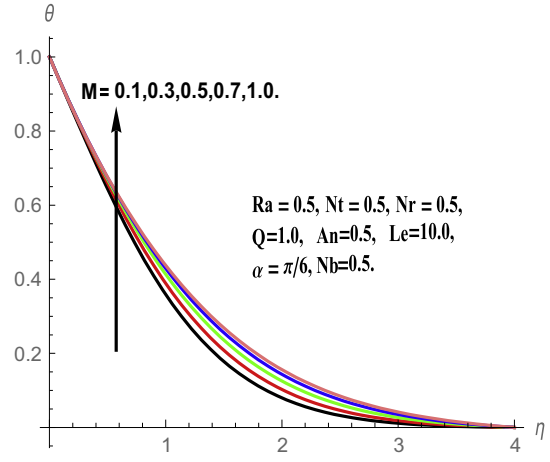

Fig. 2. Temperature profiles for different values of *M*.

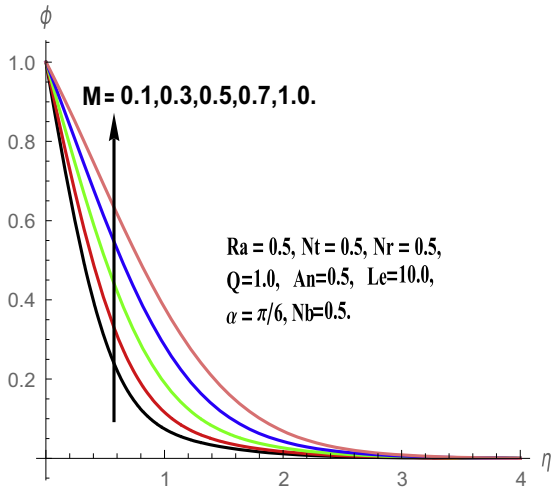

Fig. 3. Concentration profiles for different values of *M*.

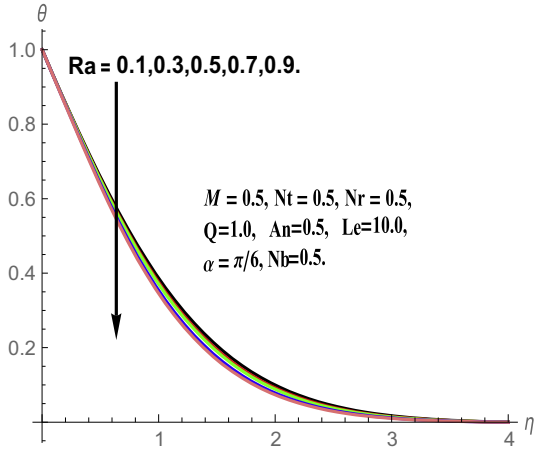

Fig. 4. Temperature profiles for different values of *Ra*.

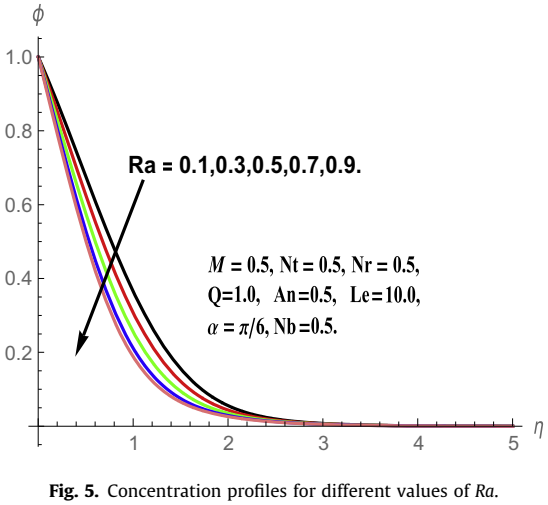

Fig. 5. Concentration profiles for different values of *Ra*.

due to the fact that, increasing the values of ($Q > 0$) in the boundary layer region creates energy as a results temperature of the fluid enhances, whereas decreasing the values of ($Q < 0$) absorbs the temperature of the fluid and is causes the deceleration in the temperature of the fluid. However, the similar opposite trend is noticed in the concentration boundary layer.

The effect of thermal radiation parameter (An) on temperature and concentration profiles is shown in Figs. 12 and 13. It is noticed form Fig. 12 that, the thermal boundary layer thickness is enhanced with the higher values of (An) in the entire flow region. This is due to the fact that imposing thermal radiation into the flow warmer the fluid, which causes an increment in the temperature of the fluid. However, there is a deceleration in the concentration boundary layer thickness with the increasing values of (An).

The effect of Brownian motion parameter (Nb) on temperature and concentration profiles is illustrated in Figs. 14 and 15. It is noticed that, with the increasing values of Brownian motion parameter (Nb) temperature profiles enhanced as shown in Fig. 14, whereas, fluid concentration profiles depreciates with enhancing values of (Nb) (Fig. 15). This type of tendency in temperature and concentration is same as in the case of general heat

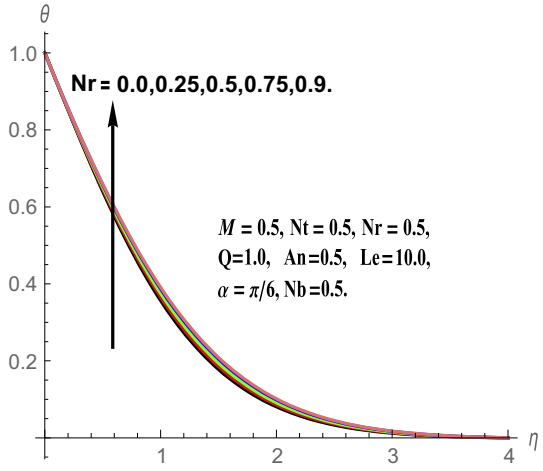

Fig. 6. Temperature profiles for different values of *Nr*.

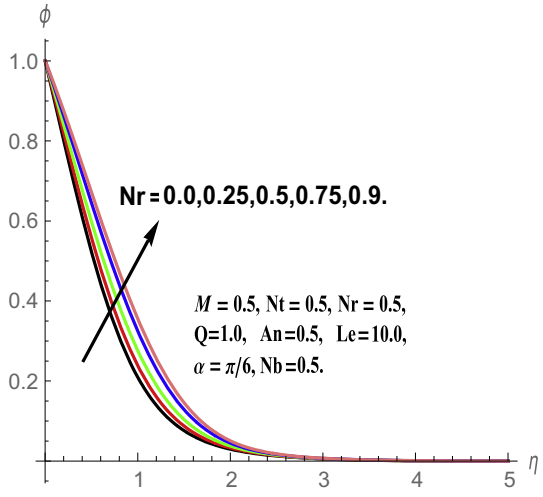

Fig. 7. Concentration profiles for different values of *Nr*.

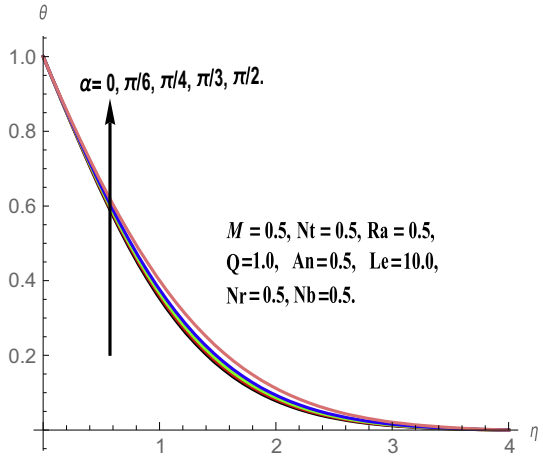

Fig. 8. Temperature profiles for different values of α.

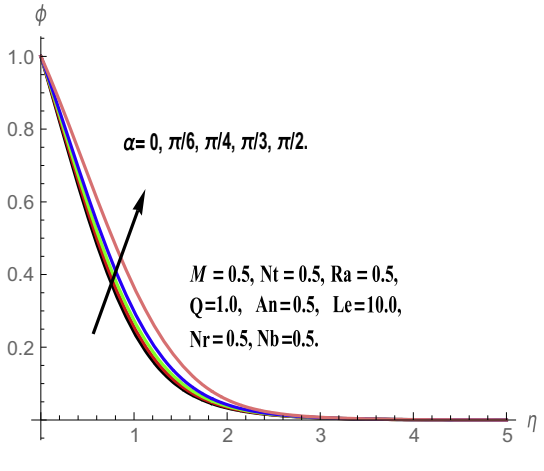

Fig. 9. Concentration profiles for different values of α.

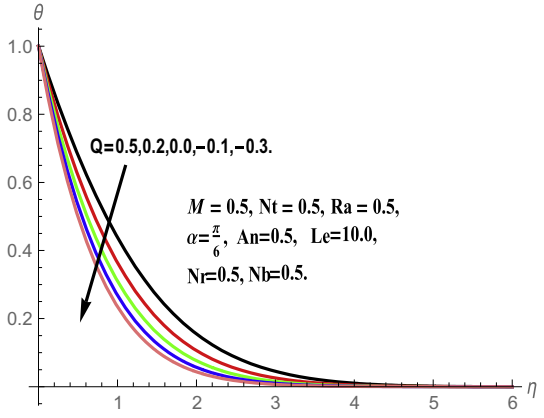

Fig. 10. Temperature profiles for different values of *Q*.

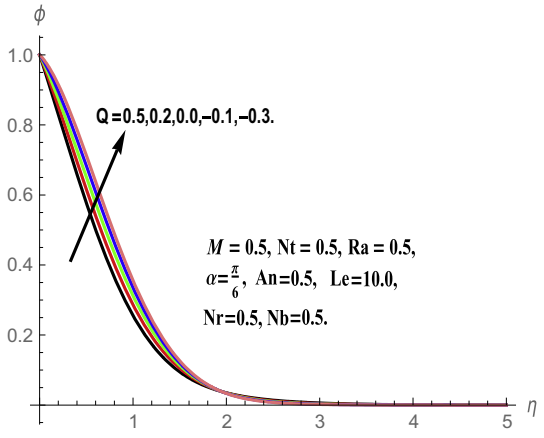

Fig. 11. Concentration profiles for different values of *Q*.

transfer fluids. Many theoretical studies suggested that, enhancement in thermal conduction of the fluid by Brownian motion of nanoparticles is because of any one of the following reasons; either nanoparticles direct effect on the fluid flow that transport heat or an indirect influence of adjacent different nanoparticles due to micro-convection of the fluid.

Variations in the thickness of thermal and solutal boundary layers for diverse values of thermophoretic parameter (*Nt*) is depicted in Figs. 16 and 17. It is noticed from these figures that both temperature and concentration profiles elevates in the boundary layer region for the higher values of thermophoretic parameter (*Nt*). This is from the reality that particles near the hot

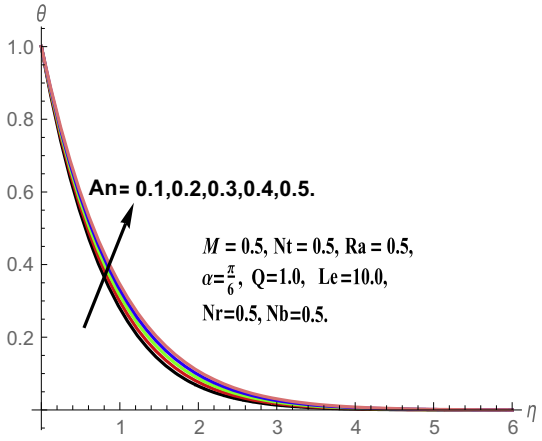

Fig. 12. Temperature profiles for different values of *An*.

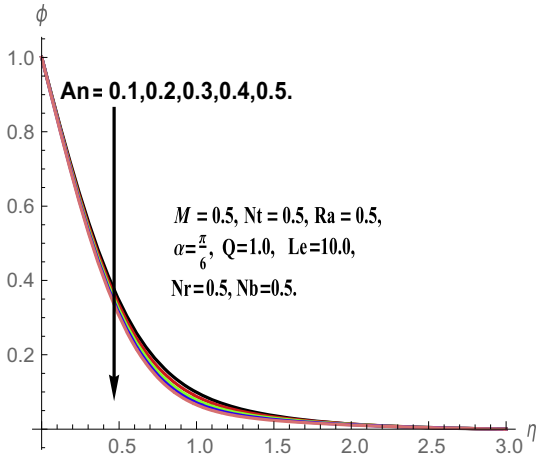

Fig. 13. Concentration profiles for different values of *An*.

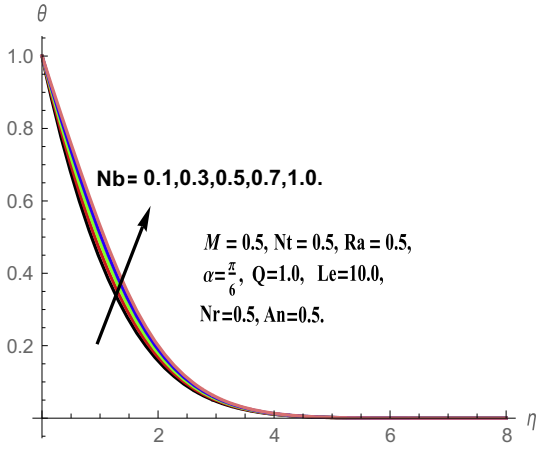

Fig. 14. Temperature profiles for different values of *Nb*.

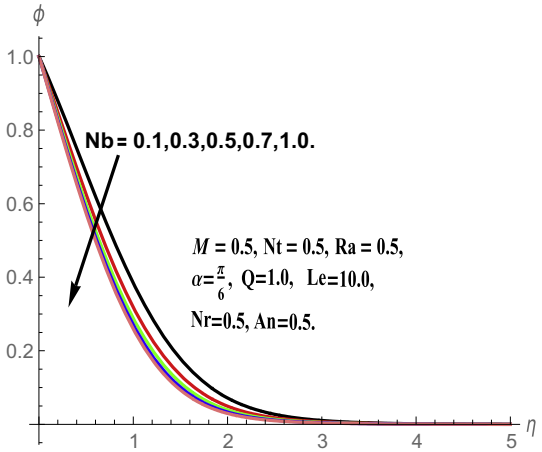

Fig. 15. Concentration profiles for different values of *Nb*.

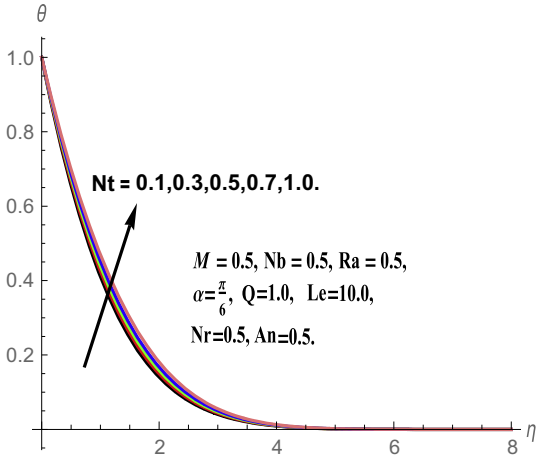

Fig. 16. Temperature profiles for different values of *Nt*.

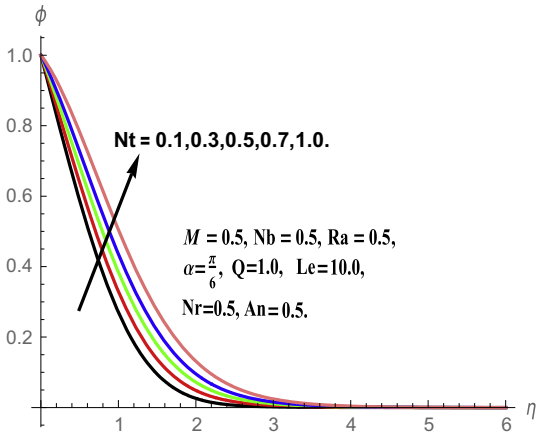

Fig. 17. Concentration profiles for different values of *Nt*.

surface create thermophoretic force; this force enhances the temperature and concentration of the fluid in the fluid region. We noticed from Fig. 16 that the temperature differences are small, this is because of the fact that thermophoretic parameter is a nanoscale parameter so that its influence is relatively less.

The impact of Lewis number (*Le*) on solutal boundary layer profiles is plotted in Fig. 18. It is observed that the concentration distributions decelerate with higher values of Lewis number (*Le*) in the entire flow region. By the definition, Lewis number can be defined as the ratio of thermal diffusivity to mass diffusivity. Lewis number increasing means higher the thermal diffusivity and lower the mass diffusivity, as a result thinner the concentration boundary layer.

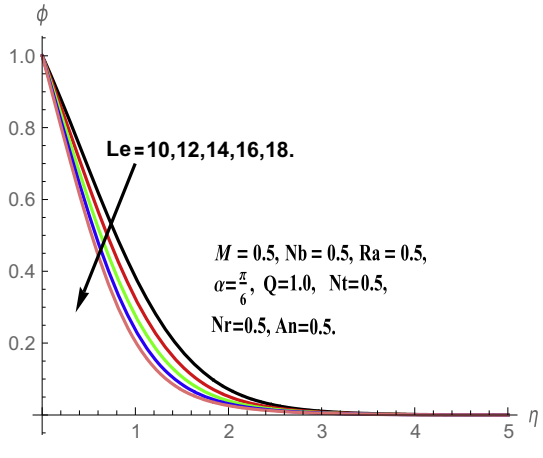

Fig. 18. Concentration profiles for different values of *Le*.

Table 2
Comparison of $(-\theta'(0))$ and $(-\phi'(0))$ with Puneet Rana et al. [28] for $Nr = 0.5$, $Ra = 1.0$, $\alpha = \pi/6$ and $M = 0$, $An = 0$, $Q = 0$.

Parameter			$-\theta'(0)$		$-\phi'(0)$	
Le	*Nb*	*Nt*	Puneet Rana et al. [28]	Present study	Puneet Rana et al. [28]	Present study
5.0	0.5	0.1	0.4425	0.4429	1.5101	1.5103
5.0	0.5	0.3	0.4064	0.4065	1.5106	1.5107
5.0	0.5	0.5	0.3742	0.3744	1.5194	1.5196
5.0	1.0	0.1	0.3025	0.3026	1.5433	1.5433
5.0	1.0	0.3	0.2779	0.2780	1.5601	1.5603
5.0	1.0	0.5	0.2559	0.2561	1.5803	1.5804
5.0	1.5	0.1	0.0879	0.0880	1.5693	1.5695
5.0	1.5	0.3	0.0807	0.0809	1.5855	1.5856
5.0	1.5	0.5	0.0742	0.0744	1.6013	1.6015
15.0	0.5	0.1	0.4298	0.4299	2.6943	2.6945
15.0	0.5	0.3	0.3933	0.3936	2.7160	2.7165
15.0	0.5	0.5	0.3609	0.3609	2.7461	2.7464
15.0	1.0	0.1	0.2823	0.2825	2.7192	2.7196
15.0	1.0	0.3	0.2579	0.2580	2.7444	2.7449
15.0	1.0	0.5	0.2366	0.2366	2.7741	2.7745
15.0	1.5	0.1	0.0747	0.0749	2.7362	2.7364
15.0	1.5	0.3	0.0683	0.0683	2.7555	2.7559
15.0	1.5	0.5	0.0626	0.0626	2.7735	2.7740

The values of Nusselt number $-\theta'(0)$ and Sherwood number $-\phi'(0)$ for different values of the important parameters are presented in Table 3. It is clear that the dimensionless heat transfer rates enhanced with increase in magnetic parameter (M), while dimensionless mass transfer rates retards with (M). The increase in mixed convection parameter (Ra) decelerates the rates of dimensionless heat transfer whereas increases the mass transfer rates. It is evident that the dimensionless heat transfer rates boosted with higher values of heat source parameter (Q). However, it is found that dimensionless mass transfer rates sinks with higher values of (Q). The dimensionless heat transfer rates deteriorate with the higher values of thermal radiation parameter (An), while reverse trend is noticed in the rates of dimensionless mass transfer in the flow region. It is clear from the table that the rates of dimensionless heat transfer declines with the increasing values both Brownian motion parameter (Nb) and thermophoresis parameter (Nt). However, the dimensionless mass transfer rates increases with the higher values of Brownian motion parameter, while it retards with increasing values of (Nt).

Table 3
The values of reduced Nusselt number $(-\theta'(0))$ and reduced Sherwood number $(-\phi'(0))$ for various values of M, Ra, Q, An, Nb, Nt.

M	*Ra*	*Q*	*An*	*Nb*	*Nt*	$-\theta'(0)$	$-\phi'(0)$
0.1	0.5	0.2	0.5	0.5	0.5	0.729015	0.823777
0.3	0.5	0.2	0.5	0.5	0.5	0.756469	0.415321
0.5	0.5	0.2	0.5	0.5	0.5	0.778888	0.190751
0.7	0.5	0.2	0.5	0.5	0.5	0.793672	0.066512
1.0	0.5	0.2	0.5	0.5	0.5	0.803198	0.007920
0.5	0.1	0.2	0.5	0.5	0.5	0.742699	0.571396
0.5	0.3	0.2	0.5	0.5	0.5	0.735439	0.697026
0.5	0.5	0.2	0.5	0.5	0.5	0.729009	0.823797
0.5	0.7	0.2	0.5	0.5	0.5	0.723578	0.949449
0.5	0.9	0.2	0.5	0.5	0.5	0.720822	1.023676
0.5	0.5	−0.3	0.5	0.5	0.5	0.729009	0.823797
0.5	0.5	−0.1	0.5	0.5	0.5	0.913578	0.677547
0.5	0.5	0.0	0.5	0.5	0.5	1.075192	0.536674
0.5	0.5	0.2	0.5	0.5	0.5	1.221194	0.401455
0.5	0.5	0.5	0.5	0.5	0.5	1.355626	0.271665
0.5	0.5	0.2	0.1	0.5	0.5	1.442845	0.414035
0.5	0.5	0.2	0.2	0.5	0.5	1.207525	0.465721
0.5	0.5	0.2	0.3	0.5	0.5	1.094852	0.508874
0.5	0.5	0.2	0.4	0.5	0.5	1.051311	0.545489
0.5	0.5	0.2	0.5	0.5	0.5	1.012862	0.576968
0.5	0.5	0.2	0.5	0.1	0.5	0.752115	0.561672
0.5	0.5	0.2	0.5	0.3	0.5	0.678755	0.742992
0.5	0.5	0.2	0.5	0.5	0.5	0.613276	0.822151
0.5	0.5	0.2	0.5	0.7	0.5	0.555051	0.865164
0.5	0.5	0.5	0.5	1.0	0.5	0.503449	0.891259
0.5	0.5	0.5	0.5	0.5	0.1	0.810861	0.845884
0.5	0.5	0.5	0.5	0.5	0.3	0.780341	0.695534
0.5	0.5	0.5	0.5	0.5	0.5	0.752137	0.561515
0.5	0.5	0.5	0.5	0.5	0.7	0.726023	0.441853
0.5	0.5	0.5	0.5	0.5	1.0	0.690345	0.285569

5. Conclusions

In this article, a theoretical study is implemented to examine the heat and mass transfer characteristics of a MHD nanofluid along an inclined vertical plate embedded in a porous medium with thermal radiation, and heat generating source. The governing partial differential equations are transformed into the set of nonlinear ordinary differential equations using similarity variables. The resulting ordinary differential equations together with boundary conditions are solved using Finite element method. The influence of magnetic field and thermal radiation parameters on temperature and concentration profiles were analyzed in detail and are presented graphically. In addition to that the reduced Nusselt and Sherwood numbers were calculated for different values of important parameters and shown in tabular form. The highlights of the present problem can be summarized as follows.

(i) Temperature and concentration profiles rises with higher values of Magnetic field parameter (M). However, the gradient of temperature enhances whereas the gradient of diffusion decelerates with increasing values of (M).
(ii) Both parameters Brownian motion (Nb) and thermophoresis (Nt) increases the thickness of the thermal boundary layer in the flow region. Whereas local Nusselt number reduces with higher values of (Nb) and (Nt).
(iii) Increasing the plate inclination angle (α) elevates the temperature and concentration distributions.
(iv) Temperature profiles enhances with increasing values of thermal radiation parameter (An), but dimensionless temperature rates denigrates and mass transfer rates enhances with (An).
(v) The temperature profiles elevate with heat generation parameter ($Q > 0$), whereas retards with heat absorption parameter ($Q > 0$).

References

[1] S.U.S. Choi, Enhancing thermal conductivity of fluids with nanoparticles, in: Proceedings of the 1995 ASME International Mechanical Engineering Congress and Exposition, San Francisco, USA, ASME, FED 231/MD, vol. 66, 1995, pp. 99–105.

[2] J.A. Eastman, S.U.S. Choi, S. Li, L.J. Thompson, S. Lee, Enhanced thermal conductivity through the development of nanofluids, in: S. Komarneni, J.C. Parker, H.J. Wollenberger (Eds.), Nanophase and Nanocomposite Materials II, MRS Pittsburg, PA, 1997, pp. 3–11.

[3] J.A. Eastman, S.U.S. Choi, S. Li, W. Yu, L.J. Thompson, Anomalously increased effective thermal conductivities of ethylene glycol-based nano-fluids containing copper nano-particles, Appl. Phys. Lett. 78 (2001) 718–720.

[4] S.U.S. Choi, Z.G. Zhang, W. Yu, F.E. Lockwood, E.A. Grulke, Anomalous thermal conductivity enhancement in nano-tube suspensions, Appl. Phys. Lett. 79 (2001) 2252–2254.

[5] H. Xie, J. Wang, T. Xi, Y. Liu, F. Ai, Q. Wu, Thermal conductivity enhancement of suspensions containing nanosized alumina particles, J. Appl. Phys. 91 (2002) 4568–4572.

[6] J. Buongiorno, Convective transport in nanofluids, ASME J. Heat Transfer 128 (2006) 240–250.

[7] D.A. Nield, A.V. Kuznetsov, The Cheng–Minkowycz problem for natural convection boundary-layer flow in a porous medium saturated by a nanofluid, Int. J. Heat Mass Transfer 52 (2009) 5792–5795.

[8] A.V. Kuznetsov, D.A. Nield, Natural convection boundary-layer of a nanofluid past a vertical plate, Int. J. Therm. Sci. 49 (2010) 243–247.

[9] W.A. Khan, I. Pop, Boundary-layer flow of a nanofluid past a stretching sheet, Int. J. Heat Mass Transfer 53 (2010) 2477–2483.

[10] A.J. Chamkha, A.M. Aly, H. Al-Mudhaf, Laminar MHD mixed convection flow of a nanofluid along a stretching permeable surface in the presence of heat generation or absorption effects, Int. J. Microscale Nanoscale Therm. Fluid Transp. Phenom 2 (2011). Article 3.

[11] P. Sudarsana Reddy, A.J. Chamkha, Soret and Dufour effects on unsteady MHD heat and mass transfer over a stretching sheet with thermophoresis and non-uniform heat generation/absorption, J. Appl. Fluid Mech. 9 (2016) 2443–2455.

[12] M.A. Hamad, I. Pop, A.I. Ismail, Magnetic field effects on free convection flow of a nanofluid past a vertical semi-infinite flat plate, Nonlinear Anal. Real World Appl. 12 (2011) 1338–1346.

[13] T. Poornima, N. Bhaskar Reddy, Radiation effects on MHD free convective boundary layer flow of nanofluids over a nonlinear stretching sheet, Adv. Appl. Sci. Res. 4 (2013) 190–202.

[14] B.J. Gireesha, A.J. Chamkha, S. Manjunatha, C.S. Bagewadi, Mixed convective flow of a dusty fluid over a vertical stretching sheet with non-uniform heat source/sink and radiation, Int. J. Numer. Meth. Heat Fluid Flow 23 (2013) 598–612.

[15] A.M. Rashad, A.J. Chamkha, S.M.M. El-Kabeir, Effects of radiation and chemical reaction on heat and mass transfer by natural convection in a micropolar fluid saturated porous medium with streamwise temperature and species concentration variations, Heat Transfer Res. 45 (2014) 795–815.

[16] M.M. Rashidi, M. Ali, N. Freidoonimehr, B. Rostami, M. Anwar Hossain, Mixed convective heat transfer for MHD visco-elastic fluid flow over a porous wedge with thermal radiation, Adv. Mech. Eng. 2014. Article number 735939.

[17] E.H. Aly, Radiation and MHD boundary layer stagnation-point of nanofluid flow towards a stretching sheet embedded in a porous medium: analysis of suction/injection and heat generation/absorption with effect of the slip model, Math. Probl. Eng. (2015), http://dx.doi.org/10.1155/2015/563547.

[18] A.J. Chamkha, A. Ben-Nakhi, MHD mixed convection - radiation interaction along a permeable surface immersed in a porous medium in the presence of Soret and Dufour effects, Heat Mass Transf. 44 (2008) 845–856.

[19] A.J. Chamkha, S. Abbasbandy, A.M. Rashad, K. Vajravelu, Radiation effects on mixed convection over a wedge embedded in a porous medium filled with a nanofluid, Transport Porous Media 91 (2012) 261–279.

[20] A. Noghrehabadi, A. Behseresht, M. Ghalambaz, Natural convection of nanofluid over vertical plate embedded porous medium, Appl. Math. Mech. (Engl. Ed.) 34 (2013) 669–686.

[21] E. Haile, B. Shankar, Heat and mass transfer in the boundary layer of unsteady viscous nanofluid along a vertical stretching sheet, J. Comput. Eng. (2014), DOI.10.1155/2014/345153.

[22] M. Ghalambaz, A. Noghrehabadi, A. Ghanbarzadeh, Natural convection of nanofluids over a convectively heated vertical plate embedded in a porous medium, Braz. J. Chem. Eng. 31 (2014) 413–427.

[23] A.J. Chamkha, S. Abbasbandy, A.M. Rashad, Non-Darcy natural convection flow of non-newtonian nanofluid over a cone saturated in a porous medium with uniform heat and volume fraction fluxes, Int. J. Numer. Meth. Heat Fluid Flow 25 (2015) 422–437.

[24] P. Sudarsana Reddy, P. Sreedevi, Ali J. Chamkha, MHD boundary layer flow, heat and mass transfer analysis over a rotating disk through porous medium saturated by Cu-water and Ag-water nanofluid with chemical reaction, Powder Technol. 307 (2017) 46–55.

[25] P. Sudarsana Reddy, K.V. Suryanarayana Rao, MHD natural convection heat and mass transfer of Al_2O_3 - water and Ag - water nanofluids over a vertical cone with chemical reaction, Proc. Eng. 127 (2015) 476–484.

[26] A.J. Chamkha, Camille Issa, Khalil Khanafer, Natural convection from an inclined plate embedded in a variable porosity porous medium due to solar radiation, Int. J. Therm. Sci. 41 (2002) 73–81.

[27] M.S. Alam, M.M. Rahman, M.A. Sattar, Similarity solutions for hydro magnetic free convective heat and mass transfer flow along a semi-infinite permeable inclined flat plate with heat generation and thermophoresis, Nonlinear Anal. Model. Control 12 (2007) 433–445.

[28] Puneet Rana, R. Bhargava, O.A. Beg, Numerical solution for mixed convection boundary layer flow of a nanofluid along an inclined plate embedded in a porous medium, Comput. Math. Appl. 64 (2012) 2816–2832.

[29] M. Rahimi-Gorji, O. Pourmehran, M. Hatami, D.D. Ganji, Statistical optimization of microchannel heat sink (MCHS) geometry cooled by different nanofluids using RSM analysis, Eur. Phys. J. Plus 130 (2) (2015) 1–21.

[30] M. Rahimi-Gorji, O. Pourmehran, M. Gorji-Bandpy, D.D. Ganji, Unsteady squeezing nanofluid simulation and investigation of its effect on important heat transfer parameters in presence of magnetic field, J. Taiwan Inst. Chem. Eng. 67 (2016) 467–475.

[31] O. Pourmehran, M. Rahimi-Gorji, M. Gorji-Bandpy, D.D. Ganji, Analytical investigation of squeezing unsteady nanofluid flow between parallel plates by LSM and CM, Alexandria Eng. J. 54 (2015) 17–26.

[32] O. Pourmehran, M. Rahimi-Gorji, M. Hatami, S.A.R. Sahebi, M. Domairry, Numerical optimization of microchannel heat sink (MCHS) performance cooled by KKL based nanofluids in saturated porous medium, J. Taiwan Inst. Chem. Eng. 55 (2015) 49–68.

[33] M. Rahimi-Gorji, O. Pourmehran, M. Gorji-Bandpy, D.D. Ganji, An analytical investigation on unsteady motion of vertically falling spherical particles in non-Newtonian fluid by Collocation Method, Ain Shams Eng. J. 6 (2) (2015) 531–540.

[34] A. Zaraki, M. Ghalambaz, A.J. Chamkha, Mehdi Ghalambaz, Danilo De Rossi, Theoretical analysis of natural convection boundary layer heat and mass transfer of nanofluids: effects of size, shape and type of nanoparticles, type of base fluid and working temperature, Adv. Powder Technol. 26 (2015) 935–946.

[35] P. Sudarsana Reddy, A.J. Chamkha, Soret and Dufour effects on MHD convective flow of Al_2O_3–water and TiO_2–water nanofluids past a stretching sheet in porous media with heat generation/absorption, Adv. Powder Technol. 27 (2016) 1207–1218.

[36] P. Sudarsana Reddy, A.J. Chamkha, Influence of size, shape, type of nanoparticles, type and temperature of the base fluid on natural convection MHD of nanofluids, Alexandria Eng. J. 55 (2016) 331–341.

[37] O. Anwar Bég, H.S. Takhar, R. Bhargava, S. Rawat, V.R. Prasad, Numerical study of heat transfer of a third grade viscoelastic fluid in non-Darcian porous media with thermophysical effects, Phys. Scr. 77 (2008) 1–11.

[38] P. Sudarsana Reddy, A.J. Chamkha, Soret and Dufour effects on unsteady MHD heat and mass transfer over a stretching sheet with thermophoresis and non-uniform heat generation/absorption, J. Appl. Fluid Mech. 9 (2016) 2443–2455.

[39] P. Rana, R. Bhargava, Flow and heat transfer of a nanofluid over a nonlinearly stretching sheet: a numerical study, Commun. Nonlinear Sci. Numer. Simulat. 17 (2012) 212–226.

[40] P. Sudarsana Reddy, A.J. Chamkha, Soret and Dufour effects on MHD heat and mass transfer flow of a micropolar fluid with thermophoresis particle deposition, J. Naval Archit. Marine Eng. 13 (2016) 39–50.